

Structural and mechanical properties of monolayer amorphous carbon and boron nitrideXi Zhang ^{1,*} Yu-Tian Zhang ^{1,2,*} Yun-Peng Wang,³ Shiyu Li,¹ Shixuan Du,^{1,4}
Yu-Yang Zhang ^{1,†} and Sokrates T. Pantelides^{5,1}¹University of Chinese Academy of Sciences and Institute of Physics, Chinese Academy of Sciences, Beijing 100049, China²CAS Key Laboratory of Theoretical Physics, Institute of Theoretical Physics, Chinese Academy of Sciences, Beijing 100190, China³Hunan Key Laboratory for Super Microstructure and Ultrafast Process, School of Physics and Electronics, Central South University, Changsha 410083, China⁴Songshan Lake Materials Laboratory, Dongguan, Guangdong 523808, China⁵Department of Physics and Astronomy and Department of Electrical and Computer Engineering, Vanderbilt University, Nashville, Tennessee 37235, USA

(Received 26 September 2023; revised 25 March 2024; accepted 23 April 2024; published 7 May 2024)

Amorphous materials exhibit various characteristics that are not featured by crystals and can sometimes be tuned by their degree of disorder (DOD). Here, we report results on the mechanical properties of monolayer amorphous carbon (MAC) and monolayer amorphous boron nitride (maBN) with different DOD. The pertinent structures are obtained by kinetic Monte Carlo (kMC) simulations using machine-learning potentials with density-functional theory-level accuracy. An intuitive order parameter, namely, the areal fraction F_x occupied by crystallites within the continuous random network, is proposed to describe the DOD. We find that F_x captures the essence of the DOD: Samples with the same F_x but different sizes and arrangements of crystallites, obtained using two distinct kMC procedures, have virtually identical radial distribution functions as well as bond-length and bond-angle distributions. Furthermore, by simulating the fracture process with molecular dynamics, we found that the mechanical responses of MAC and maBN before fracture are mainly determined by F_x and are insensitive to the sizes and specific arrangements and to some extent the numbers and area distributions of the crystallites. The behavior of cracks in the two materials is analyzed and found to mainly propagate in meandering paths in the continuous random network region and to be influenced by crystallites in distinct ways that toughen the material. The present results reveal the relation between structure and mechanical properties in amorphous monolayers and may provide a universal toughening strategy for two-dimensional materials.

DOI: [10.1103/PhysRevB.109.174106](https://doi.org/10.1103/PhysRevB.109.174106)**I. INTRODUCTION**

Two-dimensional (2D) materials exhibit unique properties. Their mechanical properties, in particular fracture toughness, which describes the ability of a material containing a crack to resist fracture, are essential for their reliable integration into future electronic, composite, and nano-electromechanical applications [1–4]. However, cracks in 2D materials generally induce brittle behavior at room temperature [5–8]. Given the brittle nature of 2D materials, it is important to investigate their mechanical properties and find effective ways to toughen them for applications. Introducing extrinsic defects and increasing the defect density is one way to increase the fracture toughness of graphene [9]. In contrast, binary materials like monolayer hexagonal boron nitride (h-BN) are intrinsically toughened by an asymmetric deformation at crack tips (due to asymmetric edge polarization) [10]. Overall, disorder engineering is an effective toughening strategy for 2D materials.

Amorphous materials that are highly disordered feature a wealth of mechanical properties [11–16], but their atomic structures are very complicated and highly debated. As a

result, the construction of structure-properties relations for amorphous materials remains a long-standing riddle. The task is simpler in 2D, as it is possible to directly determine the atomic positions by high-resolution scanning transmission electron microscopy (STEM). In 2019, monolayer amorphous carbon (MAC) was successfully synthesized for the first time and atomic-resolution STEM directly revealed that MAC is a Zachariasen continuous random network (Z-CRN) containing crystallites. It was also found that MAC exhibits high toughness [17]. More recently, in the case of MAC, the degree of disorder (DOD) was found to be tunable by the growth temperature and to affect the electrical conductivity significantly. A medium-range order (MRO) parameter, η_{MRO} , together with density of conducting sites, ρ_{sites} , are introduced to correlate properties to the DOD [18].

Monolayer amorphous BN (maBN) has not been synthesized so far (only amorphous thin films have been reported [19]). The structure of maBN has been studied by kinetic Monte Carlo (kMC) simulations using empirical potentials [20]. It was found that maBN features pseudocrystallites, i.e., honeycomb regions comprising noncanonical hexagons with random B-B and N-N bonds, in a Z-CRN [20]. Furthermore, the mechanical and thermal properties of MAC and maBN have by now also been investigated by simulations based on empirical potentials [20–23]. However,

*These authors contributed equally to this work.

†zhangyuyang@ucas.ac.cn

the accuracy of empirical potentials is never as high as that of density-functional theory (DFT) calculations, especially for binary materials. kMC simulations based on DFT evaluations of total energies for the construction of amorphous structures still remain out of reach, but the advent of practical methods for generating DFT-based machine-learning potentials opens up new opportunities to investigate the structure and properties of amorphous materials.

In this paper, we investigate the structure and mechanical properties of monolayer amorphous carbon and boron nitride using machine-learning potentials (MLPs) with DFT-level accuracy. The kMC simulation [24], a widely used sampling method for fast exploration of potential energy surfaces, was employed to assist the active-learning procedure to train the MLPs. Then the structure evolution of MAC and maBN is simulated by kMC with the bonding energetics described by the as-trained MLPs. It is found that crystallites are in fact more energetically favored within maBN than pseudocrystallites. Moreover, an intuitive order parameter, F_x , the fraction of the area occupied by crystallites, is proposed to quantify the DOD of these amorphous materials. We find that F_x captures the essence of the DOD: We demonstrate that samples with the same F_x but featuring very different atomic structures, namely, different sizes and arrangements of nanocrystallites, have essentially identical radial distribution functions and bond-angle and bond-length distributions. The same conclusions are obtained for samples with still the same F_x but are generated by a “reverse annealing” kMC procedure, namely, starting with crystalline samples, graphene, or h-BN, and using the kMC procedure to gradually amorphize them. In fact, same- F_x samples generated by the two different procedures typically differ to some extent in the numbers of crystallites and even the crystallite-area distributions. Yet, we find that, in all such MAC and maBN samples featuring very different atomic structures, the mechanical properties, namely, the stress-strain responses that define the moduli and strength, investigated by MLP-based molecular dynamics (MD) simulations, are determined by the F_x value of the sample. Though this conclusion has been validated for a wide range of same- F_x atomic structures, it may well be violated in cases of extensive differences in statistical aspects such as crystallite numbers, area distributions, etc., that may have low probability in standard kMC simulations. Moreover, we found that crack propagation exhibits very similar behaviors in MAC and maBN. Crack propagation can be regarded as the formation and the coalescence of voids. The existence of crystallites affects the locations of void formation, causing behaviors such as deflection, stopping, and bridging of cracks, which lead to rich toughening mechanisms compared with the crystalline material. The results deepen our understanding of the structure-mechanical-properties relationship in 2D amorphous materials.

II. RESULTS AND DISCUSSION

A. Construction and validation of MLPs

The MLP set is trained by using the open-source DEEPM-D-KIT package [25,26] with the training dataset collected by kMC simulation assisted active learning (Fig. S1 of the

Supplemental Material [27]). Considering the complex behavior of atoms in fracture simulation [28,29], the training dataset consists of not only amorphous configurations but also fractured samples under high tension, and even some other allotropes, and the root-mean-square error of the validation set is ~ 6 meV per atom, which is consistent with the accepted standard for accurate MLPs [30–32]. Details of the generation process are described in the Supplemental Material [27]. We first validated the reliability of the as-generated MLPs by comparing MLP- and DFT-calculated energy changes ΔE that are needed to decide whether to accept or reject Stone-Wales transformations (also nearest-neighbor B and N exchanges in maBN) during kMC procedures. Relatively small sets of randomly selected steps from the beginning to the end of the kMC simulations are chosen because the DFT calculations are computationally taxing. The comparisons for MAC and maBN are shown in Figs. 1(a) and 1(d), respectively. The energy changes calculated by MLPs are very close to those calculated by DFT. Furthermore, for the formation energies of some typical defects in graphene and h-BN (Supplemental Material [27] Tables S3 and S4) that affect kMC simulations, the MLP results are in agreement with those of DFT calculations. To validate the stretching simulations, we stretched several samples, and collected 150 MAC and 150 maBN snapshots under different strain conditions. The atomic forces of each atom are compared in Figs. 1(c) and 1(d) with the atoms near crack tips and single-atom-wide strings, which is observed in many simulations and even experiments [33,34], colored in red and blue, respectively. In addition, the traction-separation curves, which serve as a direct validation for the fracture process [35], calculated using MLPs, are compared with those obtained using DFT in Fig. S3, revealing excellent agreement. It is clear that the MLPs can describe stretched and fractured amorphous structures with DFT-level accuracy.

We also provide a benchmark of MLPs in phonon dispersions, which are relevant to the mechanical properties. As shown in Figs. 1(e) and 1(f), the calculated phonon dispersions of crystalline graphene and monolayer h-BN, using the as-generated MLPs, are in excellent agreement with the DFT results. In contrast, the calculated phonon dispersions using best-of-breed empirical potentials (AIREBO [36] for graphene and extended Tersoff [37] for h-BN) show significant deviations from the DFT results. As a result of the accurate description of acoustic phonon modes, the elastic constants and modulus of crystalline graphene and monolayer h-BN calculated by MLPs also outperform empirical potentials and are in good agreement with DFT results (Tables S1 and S2). Overall, by comparing MLPs with DFT side by side, it can be concluded that the as-generated MLPs can describe crystalline, amorphous, stretched, and fractured systems, with DFT-level accuracies that the best-of-breed empirical potentials cannot match. MLPs are slowly becoming the standard for “DFT-level” simulations and calculations for systems that cannot be handled by straight DFT calculations.

B. Generation and characterization of MAC and maBN samples

The first step is to construct a reliable atomic structure using MLPs. We performed kMC simulations [24,38] of the structural evolution of monolayer amorphous materials

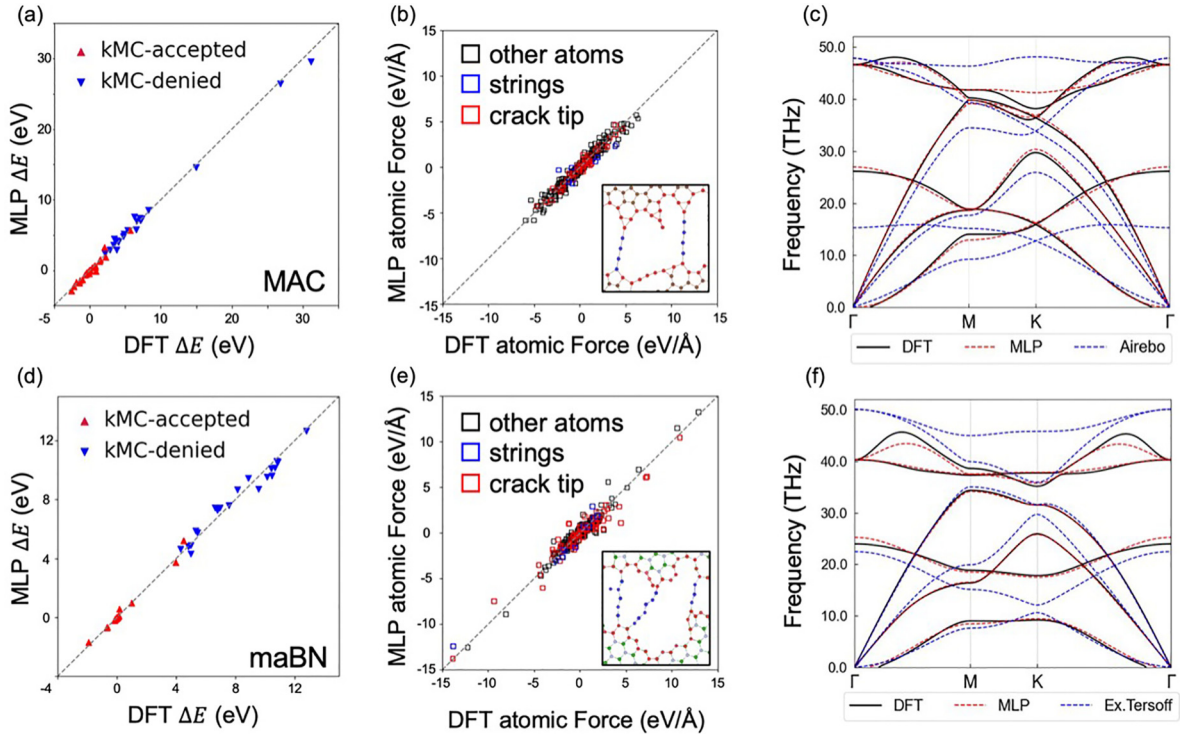


FIG. 1. Validation of MLP. (a),(d) Energy differences caused by Stone-Wales transformations or bond exchanges (only in BN systems) at randomly selected steps in the kMC algorithm. kMC-accepted ΔE 's are shown as red triangles while kMC-denied ΔE 's are shown as blue reverse triangles; (a) MAC and (d) maBN. (b),(e) Comparison of atomic forces in fractured (b) MAC and (e) maBN between DFT results and MLP predicted values. The inset is a schematic of fractured configuration, where red, blue, and black represent atoms at crack edges/tip, strings, and other regions, respectively. (c),(f) Phonon dispersion comparisons for (c) graphene and (f) h-BN, calculated using DFT (black solid), MLP (red dashed), and a state-of-the-art empirical potential (blue dashed).

(MAC and maBN). Starting from an initial configuration with randomly distributed atoms in a plane, five typical atomic structures of monolayer carbon and BN from different kMC steps are shown in Figs. 2(a) and 2(b), respectively. The canonical hexagons in crystallite islands are colored green, while noncanonical hexagons in monolayer BN are colored blue. It is worth noting that, like monolayer carbon, monolayer BN also exhibits continuously growing crystallite regions during the kMC simulation with MLP. This result contrasts with earlier findings, based on kMC simulations using an empirical potential, that monolayer amorphous BN develops exclusively pseudocrystallites, namely, honeycomb regions made up of noncanonical bonds [20]. We have now discovered that this difference arises because the extended Tersoff empirical potential substantially underestimates the energy of some noncanonical hexagons like those occurring in the recently predicted orthorhombic polymorph of BN (α - B_2N_2) [39], which directly affects the results of kMC simulations. In Table S4, we show that, unlike the empirical potential, the DFT-based MLPs reproduce the DFT-calculated formation energy of α - B_2N_2 very accurately. Thus, even though maBN contains two different elements and has a high possibility of forming noncanonical hexagons from a random distribution of atoms, the more stable, lower-energy crystallite structures prevail.

In order to distinguish amorphous structures with different DOD, an order parameter is necessary. Previously, Tian *et al.* [18] defined a DOD order parameter, η_{MRO} , namely, the ratio

of the MRO of amorphous and crystalline samples, obtained from the fluctuations of the experimental radial distribution functions (RDFs) in the medium-distance range (4–12 Å). However, in order to correlate the conductivity with the DOD, it was found necessary to introduce a second-order parameter, the density of conducting sites, ρ_{sites} , which was derived directly from atomic-scale images of MAC samples.

We explored the applicability of η_{MRO} to characterize the wide range of kMC-generated samples, i.e., individual kMC snapshots, of which Fig. 2(a) shows only five. We used MD simulations of several samples at room temperature and calculated their RDFs and η_{MRO} . We found that samples with very similar MRO and hence similar η_{MRO} may differ significantly in their short-range RDFs, their bond-angle and bond-length distributions, and even more conspicuously in the fractions of the areas occupied by crystallites (see Fig. S5 for a detailed discussion). These observations motivated us to propose an alternative and more intuitive order parameter for monolayer amorphous materials that is directly based on the atomic structure, namely, the fraction of the crystallite part of the structure, defined by

$$F_x = \frac{N_x}{N_{CRN} + N_x}.$$

Here N_x and N_{CRN} are the numbers of rings in the crystallites and the CRN regions, respectively. In practice, one canonical hexagon attached to two other adjacent canonical hexagons is counted to contribute to N_x , and all other rings

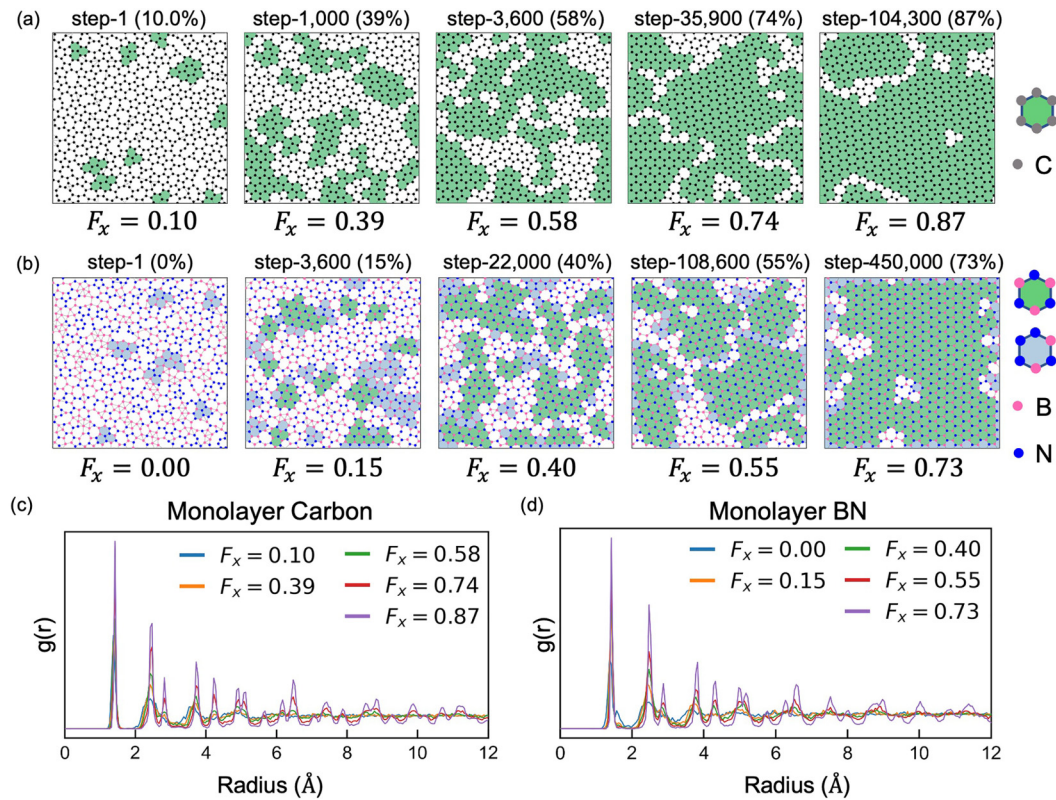


FIG. 2. Atomic structures of monolayer carbon and BN in kMC simulation. (a),(b) Atomic structures of monolayer carbon and BN from different kMC steps, respectively. The hexagons in crystallite regions are colored in green (canonical hexagons) and blue (noncanonical hexagons). The percentage of canonical hexagons (only the green region) and corresponding DOD order parameter F_x are listed. (c),(d) RDF of monolayer carbon and BN with five different F_x , respectively.

are counted to contribute to N_{CRN} (see more details in the Supplemental Material [27]). As a result, F_x ranges from 0 for the most disordered structure (fully CRN) to 1 for the most ordered structures (crystalline graphene or maBN). The calculated F_x values for samples with the same η_{MRO} are quite distinct (see Table S5). The F_x values of the five monolayer carbon samples in Fig. 2(a) are used to label their structures in Fig. 2(a) while their RDFs are shown in Fig. 2(c). All structures show clear short-range order, but their RDF peaks are broadened differently. Structures with smaller F_x exhibit broader RDF peaks and broader bond-angle and bond-length distributions, i.e., larger DOD (see Figs. S6 and S7). The five F_x values are compared with the respective η_{MRO} values in Table S6. The net conclusion is that η_{MRO} appears to be relatively insensitive to increasing DOD in samples with CRN areas that occupy more than $\sim 50\%$ of the sample, i.e., for $F_x < 0.5$.

To validate the effectiveness of F_x as a measure of the DOD, we generated four samples with completely different arrangements of crystallites, but with roughly equal values of F_x . Three samples were generated by performing the kMC procedure as in Fig. 2, i.e., starting with three different random distributions of the atoms. The fourth sample was generated by starting with a crystal and introducing disorder until the same F_x value is reached. This comparison is meant to test if the effectiveness of F_x as a measure of the DOD remains valid in the case of samples created by very different procedures. The atomic structures, RDFs, and distributions of bond

lengths and bond angles of four MAC samples with identical $F_x = 0.5$ are compared in Fig. 3. Similar comparisons are made for another two groups of MAC samples with $F_x = 0.25$ and 0.75 , in Fig. S6. Additionally, the number of crystallite islands and the crystallite-area of samples generated using different procedures are compared in Figs. S8 and S9. These figures identify some of the statistical differences of samples generated by our two different procedures. In all cases, we found that samples with very different atomic structures but the same value of F_x , i.e., samples with very different sizes and arrangements of crystallites obtained by very different procedures but having similar total crystallite areal fraction, exhibit nearly identical RDFs and distributions of bond lengths and angles. In other words, F_x captures the essential indicators of DOD.

For the binary maBN systems, the values of F_x are also calculated and shown in Fig. 2(b) while their RDFs are shown in Fig. 2(d). We also generated samples with completely different local atomic structures, but with roughly equal values of F_x , and compared their RDFs and their distributions of bond lengths and bond angles, shown in Fig. 3 and Fig. S7. Once more, we find that samples with very different atomic structures but the same value of F_x exhibit nearly identical RDFs and distributions of bond lengths and bond angles. As all the noncanonical B-B and N-N bonds are distributed in CRN regions, the areal fraction of crystallites, F_x , is able to capture both the structural and the chemical DOD in binary monolayers. We have, therefore, established F_x as an effective

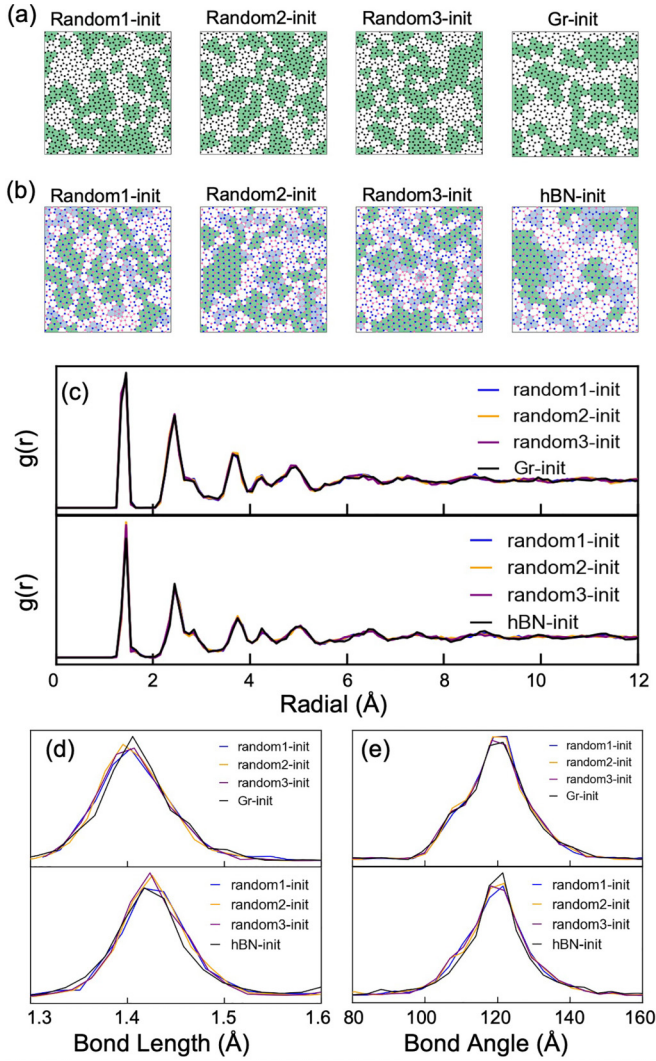


FIG. 3. Relation of F_x to different manifestations of the DOD. (a),(b) Atomic structures of four different MAC and maBN samples with identical $F_x = 0.50$ but generated from different kMC procedures (one initiates from h-BN, the other three from different random configurations). (c) RDFs of three MAC (upper panel) and maBN (lower panel) samples in (a) and (b). (d) Bond-length and (e) bond-angle distributions of the three MAC (upper panel) and three maBN (lower panel) samples in (a) and (b).

indicator (order parameter) of the DOD for 2D amorphous materials.

C. Structure-mechanical-properties relations

Admittedly, the definition of F_x as a measure of the DOD is accessible to experiments only through atomic-resolution images. However, this definition enables a detailed theoretical investigation of structure-properties relations. We have investigated the mechanical properties of MAC and maBN by performing MD simulations as follows. Structures with areas $\sim 40 \times 20 \text{ nm}^2$ were generated using the modified-building-blocks method [40]. Details are described in Figs. S10 and S11. As shown schematically in Fig. 4(c), a 2-nm-long pre-crack was introduced at the center of the model. Then, after

structural optimization and equilibration by MD for 100 ps under an NPT ensemble, a constant engineering strain was applied in the y direction until the sample breaks (a fracture develops throughout the sample). The used strain rate is 10^{-4} ps^{-1} . The NVT ensemble was used during the stretching procedure to obtain the system's response to strain and temperature fluctuations. Figure 4(a) compares the nominal 2D stress-strain relations for the mechanical response of graphene along the zigzag direction and that of MAC with different values of F_x . In the small-strain region, the stress increases smoothly as the strain is enhanced. There are two differences between crystalline and amorphous mechanical responses: (1) the stress in MAC is much lower than that of graphene at the same strain; and (2) unlike the linear stress-strain curve of graphene, the stress-strain curves of all MAC samples are nonlinear. This nonlinear stress-strain region suggests a plastic deformation in MAC samples, which is attributed to the activation of shear transformation zones (STZs). The STZs are preferentially activated in regions containing weakly bonded atoms [41–43], which refers to the CRN region in the cases of MAC and maBN. The existence of displacement vortices (Fig. S12) is the evidence of STZs' activation [44]. In a fracture process, when the strain increases to a critical value, the stress reaches its maximum and then drops, accompanied by the fracture propagation and the release of strain energy. As a typical brittle 2D material, graphene exhibits an abrupt drop in its stress-strain curve, while the stress of the MAC samples drops in a staircase fashion. Moreover, the curves in Fig. 4(a) show a sequential pattern: as the DOD increases, i.e., as F_x decreases, the critical strain increases and the maximum stress decreases. We are not ready, however, to correlate F_x with mechanical properties, because a given value of F_x can correspond to different samples with distinct atomic structures. We, therefore, compared the mechanical responses of samples with different arrangements of crystallites generated by different procedures but with similar values of F_x . Their stress-strain curves are shown in Fig. 4(d). The stress-strain curves of different samples with similar F_x are very similar to each other when the strain is smaller than the critical strain. Moreover, different structures with similar values of F_x exhibit similar critical strain and maximum stress. Therefore, our results demonstrate that the mechanical properties, i.e., strain-stress curves before fracture of kMC-generated amorphous samples are determined by F_x .

As mentioned above, the stress-strain curves of MAC exhibit kinks with abrupt drops in stress [Fig. 4(a)]. Each kink observed on the stress-strain curve indicates an initiation, propagation, or arrest of a crack. To analyze the crack behaviors near the kinks, the atomic stress distribution of a snapshot of MAC ($F_x = 0.36$) corresponding to the star mark on the stress-strain curve after the appearance of several kinks in Fig. 4(a) is shown in Fig. S13. It is found that the crack is discontinuous and is divided into three cracks, only one of which is propagating with the strain increasing, while the other two are arrested, which represents the damage tolerance of MAC samples. These simulation results are consistent with experimental data on plasticity, large toughness, and arrested crack propagation in MAC [17].

We next turn to the mechanical properties of maBN. The stress-strain curves of h-BN along the zigzag direction and

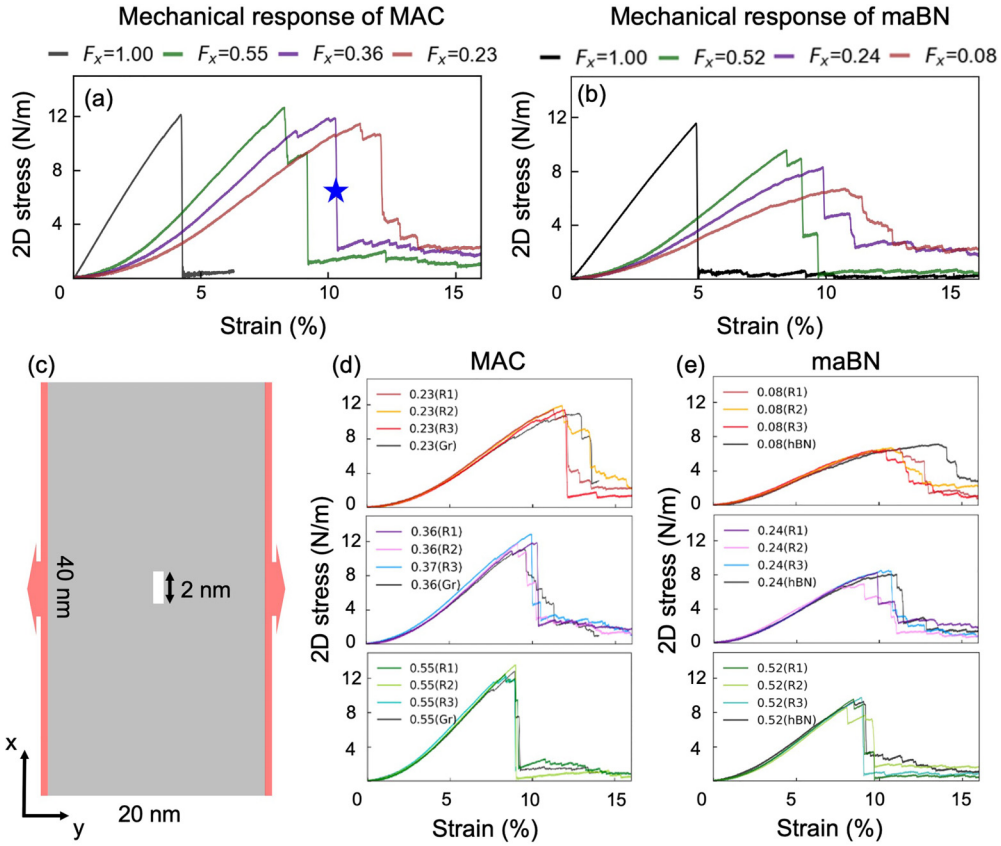


FIG. 4. Mechanical response of MAC and maBN. (a) Strain-stress curves of MAC and with three different F_x comparing with the precrack graphene along a zigzag direction. The blue star represents a snapshot containing two arrested cracks. (b) Stress-strain curves of maBN with different F_x compared with the precrack monolayer h-BN along a zigzag direction. (c) Schematic of stretching simulations. (d),(e) Strain-stress curves for three groups of (d) MAC and (e) maBN samples, respectively. Samples in each group have similar F_x values, but are generated from different procedures: one initiates from crystal, and three initiate from different random configurations, which are labeled by Gr/hBN and R1–R3, respectively, and have completely different atomic structures. Samples labeled by R1 in the legend correspond to the sample in (a) for MAC and (b) for maBN.

maBN samples with different and similar values of F_x are shown in Figs. 4(b) and 4(e). We see the maBN shares features with MAC, including the nonlinear stress-strain relation at the small-strain region and smaller critical strain at higher values of F_x . Note that, while graphene and h-BN exhibit distinct fracture properties—with graphene having an atomically smooth cracked edge [5] but h-BN lacking such smoothness [10]—they still demonstrate similar features after amorphization. Based on the present results shown in Figs. 4(b) and 4(e), we propose that the introduction of amorphousness may serve as a universal route to toughness enhancement of 2D materials.

Another obvious difference observed in the stress-strain curves of crystalline and amorphous materials is how stress decreases during the fracture process, which is associated with the propagation of cracks. In contrast to crystalline materials, stress does not immediately drop to zero in amorphous materials. Instead, the stress in MAC and maBN decreases slowly and even fluctuates.

Overall, we have described the construction of MAC and maBN samples using a kMC algorithm in two different ways: by “annealing,” namely, starting with a totally random amorphous structure that gradually develops more and larger

crystallites and by a form of “reverse annealing,” namely, starting with a crystalline structure that is gradually amorphized. We showed that in all cases, the parameter F_x is sufficient to describe the DOD and determine the mechanical properties, namely, elastic modulus and stress-strain curves prior to fracture, independent of the differences in the sizes and arrangements of the nanocrystallites and, to some extent, even the differences in the numbers of crystallites and crystallite-area distributions. The kMC-generated structures are likely to correspond to most but not necessarily all structures that can be fabricated in the laboratory. This question can be explored by experiments, while theory lacks additional, non-kMC statistical procedures to generate monolayer amorphous structures (in contrast, for bulk materials, one can melt and quench [45]).

D. The fracture process

To understand the fracture process in MAC and maBN, a detailed analysis of crack propagation was performed. Figure 5(a) shows the pathway of the main crack in one maBN sample. It is found that the crack propagates mainly through the CRN regions between crystallites. The same is also true

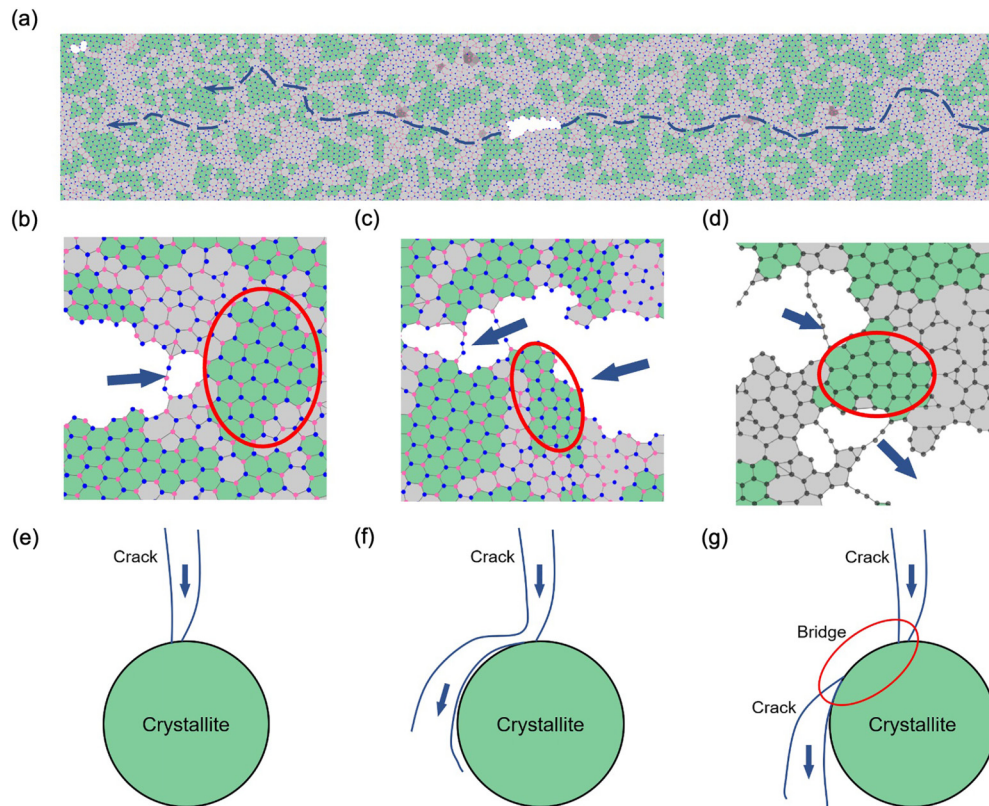


FIG. 5. Crack propagation. (a) Crack path in crystallite-maBN. The main crack interacts with crystallites in three main ways: (b),(e) crystallites stop the propagation of the main crack; (c),(f) the main crack is deflected by crystallites; and (d),(g) while the main crack is stopped by crystallite, another crack initiates near the crystallite and a bridge is formed between the two cracks.

for MAC. The randomly distributed crystallites embedded in the CRN regions result in a meandering crack path, which costs much more energy than a straight crack path like that of crystalline graphene [5]. This is because the crack propagation in the CRN region can be regarded as the formation and coalescence of voids as shown in Fig. S14, which is similar to bulk amorphous carbon [46], and the STZs, where collective atomic rearrangements occur, are preferentially activated in CRN regions where atoms are more weakly bonded than in crystallite regions. These activated STZs in the CRN are prone to exhibit elevated temperatures, facilitating the emergence of soft spots and the formation of voids within the material [47].

We next analyze the influence of crystallites on the crack propagation path. Some typical snapshots during crack propagation and corresponding schematics are shown in Figs. 5(b)–5(d). Figure 5(b) shows one blunted crack tip (blue arrows mark the direction of crack propagation) that points to a crystallite (labeled by the red circle), stops at the crystallite, and the atomic stress concentration near the stopped crack tip is partially released (Fig. S15). In contrast, voids continuously form near the crack tip shown in Fig. 5(c). As a result, this crack changes its direction and propagates along the edge of a crystallite instead of being blunted by the crystallite. In other cases, we found two cracks near a crystallite such as the snapshot shown in Fig. 5(d). One of the cracks stops in front of the crystallite just like the crack shown in Fig. 5(b). The other crack initiates from a void far from the first crack tip. The two cracks are separated by the crystallite in between forming a

crack bridge between them, resulting in a discontinuous crack path, and the crack bridge serves as a shield mechanism to protect the crack from propagating [48].

Through a detailed analysis of these snapshots, the propagation of cracks can be understood as follows. Voids are the precursors of crack tips. However, voids are very difficult to form thermally in crystallites because the formation energies of vacancies are large (7.5 eV for the vacancy in graphene) [49]. When the crack tip reaches a crystallite, there are several possible outcomes. If there is no “unstable structure” (soft spot caused by activated STZs) on either side of the crack, it is difficult to form voids near the crack tip, whereby the propagation of the crack is forced to stop [Figs. 5(b) and 5(e)]. On the contrary, if there is an unstable structure nearby, where voids can form from, the crack is deflected by the crystallite [Figs. 5(c) and 5(f)]. The deflection of the crack path increases the energy cost of crack propagation and hence toughens the materials.

Another possibility is that, after a propagating crack stops at a crystallite, voids form on the other side of the crystallite far from the crack tip, whereby they are not able to directly merge into the crack tip. In this case, a new crack tip initiates at such a void and the crystallite forms a bridge between the two cracks [Figs. 5(d) and 5(g)]. The formation of the bridge helps reduce the local stress in the wake of the crack and toughens the material [50]. Overall, embedded crystallites terminate or deflect a crack that is propagating towards them or make the crack discontinuous. A meandering crack path

increases the energy cost of crack propagation and leads to toughening of amorphous materials.

III. CONCLUSIONS

In summary, accurate MLPs for monolayer amorphous carbon and BN are trained with comprehensive sampling in the phase space by kMC-assisted active learning. Crystallites are much more energetically favorable and can easily form in maBN, suggesting that pseudocrystallites are not likely to form in nonelemental materials. An intuitive order parameter, F_x , based on the atomic structures, is proposed to quantify the DOD in amorphous materials that comprise a Z-CRN and crystallites. Its effectiveness is demonstrated in MAC and maBN. For mechanical properties, large-scale uniform MAC and maBN samples were generated using the modified-building-block method. We find that the mechanical properties, stress-strain responses that reveal modulus and strength, of these samples, generated by two different kMC procedures, are determined by F_x . With the increase of F_x , there is a noticeable downward (upward) trend in critical strain (stress), respectively (exploration of how electrical conductivity of amorphous monolayers [18] correlates with F_x , however, is beyond the scope of this paper). A high crack resistance is observed in amorphous samples during the fracture process. Our analysis of crack propagations reveals that the crack resistance is attributed to complicated crack behaviors

resulting from the presence of the crystallites in a Z-CRN amorphous structure. In disordered CRN regions, there is a soft spot induced by activated STZs, leading to the formation of voids and crack propagation. Conversely, the crystallite regions, which possess resistance to void formation, can stop or deflect crack propagation or even induce the initiation of another crack, acting as a bridge between cracks. In both MAC and maBN, these behaviors are common and contribute to the propagation of cracks in a meandering and more energetically costly manner, which indicates that amorphization can toughen the two different materials in the same way. This finding suggests that amorphization may be a universal toughening mechanism, capable of improving the mechanical properties of various 2D materials.

ACKNOWLEDGMENTS

This work was supported by the National Key R&D program of China (Grant No. 2019YFA0308500), the National Natural Science Foundation of China (Grants No. 52250402 and No. 61888102), CAS Project for Young Scientists in Basic Research (YSBR-003), and the Fundamental Research Funds for the Central Universities. A portion of the research was performed in CAS Key Laboratory of Vacuum Physics. Work at Vanderbilt was funded by the U.S. Department of Energy, Office of Science, Basic Energy Sciences, Materials Science and Engineering Division Grant No. DE-FG02-09ER46554 and by the McMinn Endowment.

-
- [1] Y. Kim, J. Lee, M. S. Yeom, J. W. Shin, H. Kim, Y. Cui, J. W. Kysar, J. Hone, Y. Jung, S. Jeon, and S. M. Han, Strengthening effect of single-atomic-layer graphene in metal-graphene nanolayered composites, *Nat. Commun.* **4**, 2114 (2013).
- [2] C. Lee, X. Wei, J. W. Kysar, and J. Hone, Measurement of the elastic properties and intrinsic strength of monolayer graphene, *Science* **321**, 385 (2008).
- [3] S. Kim, J. Yu, and A. M. van der Zande, Nano-electromechanical drumhead resonators from two-dimensional material bimorphs, *Nano Lett.* **18**, 6686 (2018).
- [4] B. Ni, D. Steinbach, Z. Yang, A. Lew, B. Zhang, Q. Fang, M. J. Buehler, and J. Lou, Fracture at the two-dimensional limit, *MRS Bull.* **47**, 848 (2022).
- [5] P. Zhang, L. Ma, F. Fan, Z. Zeng, C. Peng, P. E. Loya, Z. Liu, Y. Gong, J. Zhang, X. Zhang *et al.*, Fracture toughness of graphene, *Nat. Commun.* **5**, 3782 (2014).
- [6] T. Zhang and H. Gao, Toughening graphene with topological defects: A perspective, *J. Appl. Mech.* **82**, 051001 (2015).
- [7] A. Shekhawat and R. O. Ritchie, Toughness and strength of nanocrystalline graphene, *Nat. Commun.* **7**, 10546 (2016).
- [8] Y. Yang, X. Li, M. Wen, E. Hacopian, W. Chen, Y. Gong, J. Zhang, B. Li, W. Zhou, P. M. Ajayan *et al.*, Brittle fracture of 2D MoSe₂, *Adv. Mater.* **29**, 1604201 (2017).
- [9] G. Lopez-Polin, J. Gomez-Herrero, and C. Gomez-Navarro, Confining crack propagation in defective graphene, *Nano Lett.* **15**, 2050 (2015).
- [10] Y. Yang, Z. Song, G. Lu, Q. Zhang, B. Zhang, B. Ni, C. Wang, X. Li, L. Gu, X. Xie *et al.*, Intrinsic toughening and stable crack propagation in hexagonal boron nitride, *Nature (London)* **594**, 57 (2021).
- [11] J. Robertson, Mechanical properties and coordinations of amorphous carbons, *Phys. Rev. Lett.* **68**, 220 (1992).
- [12] C. Fan, C. Li, A. Inoue, and V. Haas, Deformation behavior of Zr-based bulk nanocrystalline amorphous alloys, *Phys. Rev. B* **61**, R3761 (2000).
- [13] Z. P. Lu, C. T. Liu, J. R. Thompson, and W. D. Porter, Structural amorphous steels, *Phys. Rev. Lett.* **92**, 245503 (2004).
- [14] V. I. Ivashchenko, P. E. A. Turchi, and V. I. Shevchenko, Simulations of the mechanical properties of crystalline, nanocrystalline, and amorphous SiC and Si, *Phys. Rev. B* **75**, 085209 (2007).
- [15] C. A. Schuh, T. C. Hufnagel, and U. Ramamurty, Mechanical behavior of amorphous alloys, *Acta Mater.* **55**, 4067 (2007).
- [16] M. Zhu, J. Zhou, Z. He, Y. Zhang, H. Wu, J. Chen, Y. Zhu, Y. Hou, H. Wu, and Y. Lu, Ductile amorphous boron nitride microribbons, *Mater. Horiz.* **10**, 4914 (2023).
- [17] C. T. Toh, H. Zhang, J. Lin, A. S. Mayorov, Y. P. Wang, C. M. Orofeo, D. B. Ferry, H. Andersen, N. Kakenov, Z. Guo *et al.*, Synthesis and properties of free-standing monolayer amorphous carbon, *Nature (London)* **577**, 199 (2020).
- [18] H. Tian, Y. Ma, Z. Li, M. Cheng, S. Ning, E. Han, M. Xu, P. F. Zhang, K. Zhao, R. Li *et al.*, Disorder-tuned conductivity in amorphous monolayer carbon, *Nature (London)* **615**, 56 (2023).
- [19] S. Hong, C. S. Lee, M. H. Lee, Y. Lee, K. Y. Ma, G. Kim, S. I. Yoon, K. Ihm, K. J. Kim, T. J. Shin *et al.*, Ultralow-dielectric-

- constant amorphous boron nitride, *Nature (London)* **582**, 511 (2020).
- [20] Y. T. Zhang, Y. P. Wang, X. Zhang, Y. Y. Zhang, S. Du, and S. T. Pantelides, Structure of amorphous two-dimensional materials: Elemental monolayer amorphous carbon versus binary monolayer amorphous boron nitride, *Nano Lett.* **22**, 8018 (2022).
- [21] L. C. Felix, R. M. Tromer, P. A. S. Autreto, L. A. Ribeiro Junior, and D. S. Galvao, On the mechanical properties and thermal stability of a recently synthesized monolayer amorphous carbon, *J. Phys. Chem. C* **124**, 14855 (2020).
- [22] W. Xie and Y. Wei, Roughening for strengthening and toughening in monolayer carbon based composites, *Nano Lett.* **21**, 4823 (2021).
- [23] Y.-T. Zhang, Y.-P. Wang, Y.-Y. Zhang, S. Du, and S. T. Pantelides, Thermal transport of monolayer amorphous carbon and boron nitride, *Appl. Phys. Lett.* **120**, 222201 (2022).
- [24] F. Ding and B. I. Yakobson, Energy-driven kinetic Monte Carlo method and its application in fullerene coalescence, *J. Phys. Chem. Lett.* **5**, 2922 (2014).
- [25] H. Wang, L. Zhang, J. Han, and E. W., DeePMD-kit: A deep learning package for many-body potential energy representation and molecular dynamics, *Comput. Phys. Commun.* **228**, 178 (2018).
- [26] L. Zhang, J. Han, H. Wang, R. Car, and E. W., Deep potential molecular dynamics: A scalable model with the accuracy of quantum mechanics, *Phys. Rev. Lett.* **120**, 143001 (2018).
- [27] See Supplemental Material at <http://link.aps.org/supplemental/10.1103/PhysRevB.109.174106> for the details of the simulation method, dataset generation, potential training and validation, order parameter analysis, and additional simulation results of mechanical properties. The Supplemental Material also contains Refs. [51–58].
- [28] J. A. Hauch, D. Holland, M. P. Marder, and H. L. Swinney, Dynamic fracture in single crystal silicon, *Phys. Rev. Lett.* **82**, 3823 (1999).
- [29] L. Pastewka, A. Klemenz, P. Gumbsch, and M. Moseler, Screened empirical bond-order potentials for Si-C, *Phys. Rev. B* **87**, 205410 (2013).
- [30] M. A. Caro, G. Csányi, T. Laurila, and V. L. Deringer, Machine learning driven simulated deposition of carbon films: From low-density to diamondlike amorphous carbon, *Phys. Rev. B* **102**, 174201 (2020).
- [31] N. Xu, Y. Shi, Y. He, and Q. Shao, A deep-learning potential for crystalline and amorphous Li–Si alloys, *J. Phys. Chem. C* **124**, 16278 (2020).
- [32] G. Sivaraman, A. N. Krishnamoorthy, M. Baur, C. Holm, M. Stan, G. Csányi, C. Benmore, and Á. Vázquez-Mayagoitia, Machine-learned interatomic potentials by active learning: Amorphous and liquid hafnium dioxide, *npj Comput. Mater.* **6**, 104 (2020).
- [33] C. Cao, S. Mukherjee, J. Y. Howe, D. D. Perovic, Y. Sun, C. V. Singh, and T. Filleter, Nonlinear fracture toughness measurement and crack propagation resistance of functionalized graphene multilayers, *Sci. Adv.* **4**, eaao7202 (2018).
- [34] S. Wang, Z. Qin, G. S. Jung, F. J. Martin-Martinez, K. Zhang, M. J. Buehler, and J. H. Warner, Atomically sharp crack tips in monolayer MoS₂ and their enhanced toughness by vacancy defects, *ACS Nano* **10**, 9831 (2016).
- [35] M. Qamar, M. Mrovec, Y. Lysogorskiy, A. Bochkarev, and R. Drautz, Atomic cluster expansion for quantum-accurate large-scale simulations of carbon, *J. Chem. Theory Comput.* **19**, 5151 (2023).
- [36] S. J. Stuart, A. B. Tutein, and J. A. Harrison, A reactive potential for hydrocarbons with intermolecular interactions, *J. Chem. Phys.* **112**, 6472 (2000).
- [37] J. H. Los, J. M. H. Kroes, K. Albe, R. M. Gordillo, M. I. Katsnelson, and A. Fasolino, Extended Tersoff potential for boron nitride: Energetics and elastic properties of pristine and defective h-BN, *Phys. Rev. B* **96**, 184108 (2017).
- [38] Z. El-Machachi, M. Wilson, and V. L. Deringer, Exploring the configurational space of amorphous graphene with machine-learned atomic energies, *Chem. Sci.* **13**, 13720 (2022).
- [39] S. Demirci, S. E. Rad, S. Kazak, S. Nezir, and S. Jahangirov, Monolayer diboron dinitride: Direct band-gap semiconductor with high absorption in the visible range, *Phys. Rev. B* **101**, 125408 (2020).
- [40] B. Cai, X. Zhang, and D. A. Drabold, Building block modeling technique: Application to ternary chalcogenide glasses g-Ge₂As₄Se₄ and g-AsGe_{0.8}Se_{0.8}, *Phys. Rev. B* **83**, 092202 (2011).
- [41] H. W. Sheng, W. K. Luo, F. M. Alamgir, J. M. Bai, and E. Ma, Atomic packing and short-to-medium-range order in metallic glasses, *Nature (London)* **439**, 419 (2006).
- [42] J. Ding, S. Patinet, M. L. Falk, Y. Cheng, and E. Ma, Soft spots and their structural signature in a metallic glass, *Proc. Natl. Acad. Sci. USA* **111**, 14052 (2014).
- [43] E. Ma, Tuning order in disorder, *Nat. Mater.* **14**, 547 (2015).
- [44] D. Şopu, A. Stukowski, M. Stoica, and S. Scudino, Atomic-level processes of shear band nucleation in metallic glasses, *Phys. Rev. Lett.* **119**, 195503 (2017).
- [45] V. Rosato, M. Celino, and L. Colombo, On the effect of quench rate on the structure of amorphous carbon, *Comput. Mater. Sci.* **10**, 67 (1998).
- [46] S. M. Khosrownejad, J. R. Kermode, and L. Pastewka, Quantitative prediction of the fracture toughness of amorphous carbon from atom-scale simulations, *Phys. Rev. Mater.* **5**, 023602 (2021).
- [47] F. Moitzi, D. Şopu, D. Holec, D. Perera, N. Mousseau, and J. Eckert, Chemical bonding effects on the brittle-to-ductile transition in metallic glasses, *Acta Mater.* **188**, 273 (2020).
- [48] D. Kiener and S. M. Han, 100 years after Griffith: From brittle bulk fracture to failure in 2D materials, *MRS Bull.* **47**, 792 (2022).
- [49] M. D. Bhatt, H. Kim, and G. Kim, Various defects in graphene: A review, *RSC Adv.* **12**, 21520 (2022).
- [50] R. O. Ritchie, The conflicts between strength and toughness, *Nat. Mater.* **10**, 817 (2011).
- [51] Y. Wei, J. Wu, H. Yin, X. Shi, R. Yang, and M. Dresselhaus, The nature of strength enhancement and weakening by pentagon-heptagon defects in graphene, *Nat. Mater.* **11**, 759 (2012).
- [52] S. Plimpton, Fast parallel algorithms for short-range molecular dynamics, *J. Comput. Phys.* **117**, 1 (1995).
- [53] J. Behler and M. Parrinello, Generalized neural-network representation of high-dimensional potential-energy surfaces, *Phys. Rev. Lett.* **98**, 146401 (2007).
- [54] J. Behler, Atom-centered symmetry functions for constructing high-dimensional neural network potentials, *J. Chem. Phys.* **134**, 074106 (2011).
- [55] Y. Zhang, H. Wang, W. Chen, J. Zeng, L. Zhang, H. Wang, and E. W., DP-GEN: A concurrent learning platform for the gener-

- ation of reliable deep learning based potential energy models, *Comput. Phys. Commun.* **253**, 107206 (2020).
- [56] G. Kresse and J. Furthmüller, Efficiency of ab-initio total energy calculations for metals and semiconductors using a plane-wave basis set, *Comput. Mater. Sci.* **6**, 15 (1996).
- [57] J. P. Perdew, K. Burke, and M. Ernzerhof, Generalized gradient approximation made simple, *Phys. Rev. Lett.* **77**, 3865 (1996).
- [58] L. Zhang, J. Han, H. Wang, W. Saidi, R. Car, and W. E, End-to-end symmetry preserving inter-atomic potential energy model for finite and extended systems, in *Advances in Neural Information Processing Systems 31*, edited by S. Bengio, H. Wallach, H. Larochelle, K. Grauman, N. Cesa-Bianchi, and R. Garnett (Curran Associates, Red Hook, NY, 2018), pp. 4436–4446.